ORIGINAL RESEARCH ARTICLE

High Temperature Tensile Properties of TiN-Reinforced 17-4 PH Stainless Steel Produced by Laser Powder-Bed Fusion

ANDAC OZSOY, EDA AYDOGAN, and ARCAN F. DERICIOGLU

In this study, the effect of TiN particle reinforcements on high temperature tensile behavior of laser powder-bed fusion processed 17-4 PH stainless steel has been investigated. Tensile tests have been conducted at room temperature (RT), 400 °C, and 600 °C. It was observed that the TiN incorporation increased the strength at RT and 400 °C with a slight tradeoff in elongation. However, at 600 °C, yield and tensile strength values were lower for the composite than those of the unreinforced steel matrix, yet with a threefold increase in elongation. Further investigation on the ruptured specimens revealed that dynamic recovery, recrystallization, and phase transformation were responsible for this behavior. It has been concluded that dispersion hardening offers advantages both at room and elevated temperatures, especially in the ranges where the original alloy is normally used. However, the physical characteristics of the matrix become dominant at high temperatures ($> 0.5\ T_m$), setting an upper bound to the possible contribution of the reinforcement to a selected matrix, yet, enabling for higher ductility.

https://doi.org/10.1007/s11661-025-07721-8
© The Author(s) 2025

I. INTRODUCTION

17-4 precipitation hardening (PH) stainless steel is an important engineering material, as it offers high strength, corrosion resistance, and weldability. It is usually solutionized and aged to obtain a martensitic microstructure with finely distributed Cu-rich precipitates which provide high strength. It is workable and machinable in solutionized condition as the low-carbon martensite has relatively low hardness compared to high-carbon variants.[1] 17-4 PH stainless steel is used in various fields, such as aerospace, energy, chemical, and naval industries.[2–4] It also retains its high strength at elevated temperatures. However, its strength rapidly drops due to coarsening of the Cu-rich precipitates at temperatures above 400 °C.[2] Thus, more expensive nickel- and cobalt-based superalloys are usually utilized above these temperatures.

Laser Powder-bed Fusion (LPBF) is one of the most commonly utilized additive manufacturing (AM) methods for producing complex-shaped metallic engineering products. LPBF operates by fusion of successive layers of metal powders by a laser heat source according to the computer-aided design (CAD) data. It offers various advantages as it allows for production of lightweight and complex shapes with high dimensional accuracy. LPBF yields complex thermal histories with extremely high cooling rates (10^4 to 10^6 °C/s) and intrinsic heat treatment effect, which leads to the formation of microstructures different than wrought alloys. 17-4 PH stainless steel is one of those alloys sensitive to the small changes in chemical composition and processing conditions. As reported in the literature, 17-4 PH stainless steel shows a range of phase constitutions, such as dominantly ferritic,[5,6] dominantly austenitic,[7] ferritic-austenitic[8] or martensitic-austenitic[7,9–11] depending on the exact chemical composition of the alloy and AM processing conditions. It has been shown that the chemical composition plays a major role in determining the final microstructure, where slight variations within the standard chemical specifications of 17-4 PH stainless steel together with the variations in the process parameters can lead to completely different results which are combinations of ferrite, austenite, and martensite phases.[12,13] In addition, distinguishing low-carbon martensite from ferrite possesses difficulties as they both have a BCC structure. In such cases, the morphology of ferrite and martensite, as well as their crystallographic relation to austenite grains become the determining factor.[14]

Another important advantage of LPBF is its ability to successfully produce metal matrix composites (MMCs). Due to the tunability of the powder feedstock, LPBF eliminates the need for complicated mold designs and minimizes the required post machining processes while

ANDAC OZSOY, EDA AYDOGAN, and ARCAN F. DERICIOGLU are with the Department of Metallurgical and Materials Engineering, Middle East Technical University, 06800 Ankara, Turkey. Contact e-mail: arcan@metu.edu.tr
Manuscript submitted July 17, 2024; accepted February 10, 2025.

Published online: 20 February 2025

reducing costs and lead time.[15] Combining these advantages with the freedom of design, LPBF of MMCs has gained much interest in the relevant literature.[16–21] Dispersion strengthened materials, *i.e.*, insoluble particle reinforced metal matrix composites, have long been effective tools to increase the high temperature strength of the conventional alloys.[22] Unlike precipitates, dispersed particles usually do not dissolve in the matrix or coarsen at elevated temperatures. Therefore, they keep serving as barriers to dislocations and maintain the strength. It has been previously shown that TiN nano-particle-reinforced 17-4 PH stainless steel exhibits both increased strength and ductility at room temperature (RT) due to the combined advantage of dispersion strengthening and grain refinement.[23] In this study, high temperature tensile behavior of TiN-reinforced 17-4 PH stainless steel has been investigated, and the results have been discussed to obtain a fundamental understanding of the high temperature behavior of MMCs, so that enhanced dispersion strengthened materials could be obtained in future studies.

II. EXPERIMENTAL PROCEDURE

Commercial 17-4 PH stainless steel powders with a size distribution of 22 to 50 μm were used as the matrix, while 99.2 pct pure cubic TiN particles with a mean size of 20 nm were used as the reinforcement. Chemical composition of the 17-4 PH stainless steel powders is shown in Table I. The details of the preparation of the powder feedstock can be found elsewhere.[23] Renishaw AM400 (Wotton-under-Edge, United Kingdom) LPBF equipment with a single pulsed-wave Yb-fiber laser was used to produce cylindrical specimens lying along the build direction (parallel to the laser beam) with a diameter of 8 mm, which were then machined into tensile coupons with a gauge diameter of 4 mm per ASTM E-8 m.[24] Nitrogen was used during all builds to prevent decomposition of TiN, and optimized LPBF parameters were used to obtain relative densities above 99.5 pct as presented in Reference 23. Three coupons for each testing temperature were fabricated using unreinforced 17-4 PH stainless steel powders to produce control specimens, as well as with TiN-reinforced powders to produce composite specimens. The parameters used for both specimen types are shown in Table II. An example build can be seen in Figure 1.

Table I. Chemical Composition of the 17-4 PH Stainless Steel Powders

Element	Amount (Wt Pct)
Cr	17.39
Ni	4.12
Cu	4.53
Nb	0.33
C*	0.01
N*	0.01
Fe	bal.

*Denoted elements were taken from the vendor datasheet.

All specimens were solutionized at 1040 °C for 1 hour, cooled under pressurized argon and subsequently aged at 480 °C for 1 hour corresponding to H900 condition per ASTM A-564.[25] Extra sections and the ruptured parts of the specimens were cut, mounted, and ground to obtain a mirror-like finish. Specimens were examined under optical microscope (Axioscope 5, Carl Zeiss AG, Oberkochen) and scanning electron microscope (SEM) (Nova NanoSEM 430, FEI, Hilsboro, Oregon) equipped with an energy dispersive X-ray spectrometer (EDS) (EDAX, Mahwah, New Jersey) and an electron backscatter diffractometer (EBSD) (TSL OIM, Sagamihara). Viella's Reagent was used to reveal the grain boundaries of the control specimen, and the grain structure of the composite specimens was observed *via* EBSD, where the step size was varied between 0.05 and 0.2 μm. Hardness measurements were done using DuraJet G5 hardness testing equipment (EMCO-TEST, Kuchl) with a Rockwell indenter. Tensile tests were conducted using Instron 5582 Universal Testing Machine with a high temperature furnace attachment and an Instron 2632-057 high temperature extensometer. Tests were conducted at room temperature (RT), 400 °C, and 600 °C where all tests were conducted at a constant crosshead speed of 1 mm/min. The equilibrium phase amounts have been calculated using JMatPro® v12 software, which utilizes the well-known CALPHAD method.[26,27] Moreover, Scheil-Gulliver solidification calculations have been performed using this software to predict the phase constitutions in as-built condition. *In situ* X-ray diffraction (XRD) measurements have been conducted at room temperature (RT), 350 °C, and 600 °C using Empyrean (Malvern Panalytical, Grovewood Rd) X-ray diffractometer.

III. RESULTS

A. *Microstructure After Heat Treatment*

Figure 2(a) shows the microstructure of a control specimen after heat treatment. As shown in the figure, a martensitic microstructure with blocks and sub-blocks of lath martensite has been obtained after heat treatment, and the resulting hardness has been measured to be 42 HRC, complying with the standard requirements.[25]

The microstructure of the composite specimens in as-built condition exhibits a fine and equiaxed appearance [Figure 2(b)], implying that separate nucleation of each grain took place during solidification. As shown in Figure 2(c), a median grain size of 1.2 μm has been obtained in as-built condition. It is presumed that TiN particles acted as heterogeneous nucleation sites for the matrix grains thanks to their low lattice misfit with both austenite and ferrite.[28] It is also known that TiN does not melt or dissolve in steel melts as it has a high melting point of 2950 °C and high thermodynamic stability.[28–30] Therefore, it has been successfully used as a grain refiner in AM for both austenitic,[31] ferritic[32] and martensitic[33] steels in the literature. To evidence that they acted as nucleants, TiN particles in the composite

Table II. Process Parameters Used in the Study for Composite and Control Specimens

Parameter Set	Power (W)	Point Distance (μm)	Hatch Distance (μm)	Exposure Time (μs)	Layer Thickness (μm)
Control Specimens	200	110	110	142	30
Composite Specimens	200	50	80	66	30



Fig. 1—Image of an example build of composite specimens with the characteristic yellow tint of TiN addition.

specimens have been observed under SEM. As seen in Figure 2(d), TiN particles are embedded at the center of the grains and at the grain boundaries as cubic particles, as shown by red and dashed-white arrows, respectively. This has been also confirmed by the EDS results as their Ti concentration is significantly higher. As the interaction volume of the electron beam at 30 kV is presumably larger than the particles themselves, only a relative difference between the compositions of the matrix and the particles can be resolved *via* EDS measurements.

The appearance of the microstructure after heat treatment (H900) has not changed remarkably, a similar microstructure with a mean grain size of 2 μm has been obtained [see Figure 2(d)]. Some grain growth has occurred, since the resulting grain size distribution is somewhat non-uniform as shown in Figures 2(e) and (f). For both as-built and H900 heat-treated condition of the composite, only a BCC phase could be detected *via* EBSD. Hardness values have been found to be 37 HRC and 47 HRC for the composite specimen before and after H900 heat treatment, respectively, indicating that the microstructure with small grain size and incorporated TiN particles was further hardened by Cu-rich precipitates after the heat treatment.

B. *High Temperature Tensile Behavior*

As shown in the stress-strain diagrams in Figure 3(a) and the overall strength and elongation values given in Figure 3(b), the control specimens comply with the standard strength requirements at RT with a slightly lower elongation value than required.[25] At RT, the composite specimen exhibits higher strength values compared to the standard values with a further tradeoff in elongation. The room temperature mechanical properties were extensively discussed previously,[23] therefore, this discussion will not be repeated here. The composite shows higher strength with slightly lower elongation at 400 °C compared to the control specimen. Average yield strength, tensile strength, and elongation values are, respectively, + 20.6, + 13.4, and − 31.8 pct different than those of the control specimen, as shown in Figure 3(b). TiN addition has increased the strength approximately by 200 MPa at this temperature.

Contrary to the initial trend, the composite exhibits slightly lower strength, but much higher elongation than the control specimens at 600 °C as can be observed in Figure 3(a). As shown in Figure 3(b), average yield strength, tensile strength, and elongation values have been − 5.1, − 13.6, and + 233.3 pct different than those of the control specimen at 600 °C, respectively. A slight drop in elongation at elevated temperatures has been observed for the control specimens, contrary to the expected behavior.

C. *Post-mortem Analysis*

Figures 4(a) and (b) show the fracture surfaces of the control specimens tested at 400 °C and 600 °C, respectively. The fracture appears to be an intergranular dimpled fracture, where fracture occurred due to void coalescence at the grain boundaries (GBs). Figures 4(c) and (d) show the fracture surfaces of the composite specimens at 400 °C and 600 °C, respectively. Contrary to the control specimens, the composite specimens show the typical features of a ductile fracture at both temperatures with many dimples visible at the fracture surface. Secondary particles are visible [see Figure 4(d)] at the center of the dimples, as often observed in ductile fracture.

As shown in Figure 3(b), the composite specimens exhibit approximately three times higher elongation at 600 °C compared to the control specimens. In order to understand the mechanism behind this phenomenon, EBSD maps have been collected from the ruptured sections of the composite coupons tested at 600 °C as indicated in Figure 5(a). As can be seen in Figure 5(b), equiaxed and small-sized (< 1 μm) recrystallized grains with a distinct orientation are visible around larger and deformed grains, implying nucleation of fresh grains. On the other hand, sub-grain formation and separation into low-angle grain boundaries (LAGB) in some regions

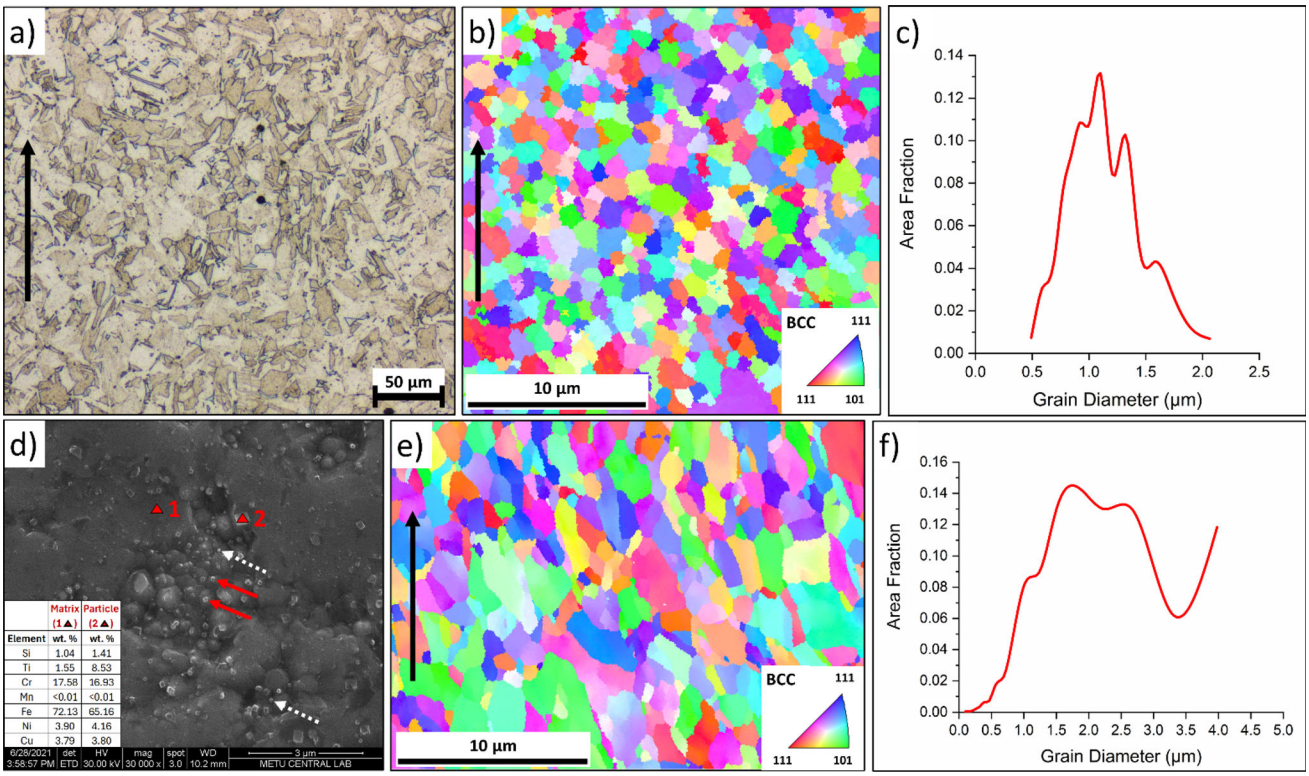

Fig. 2—(*a*) Side view optical micrograph of the control specimen after heat treatment, (*b*) EBSD IPF map of the composite specimen in as-built condition and the corresponding, (*c*) grain size distribution and (*d*) SEM image. (*e*) EBSD IPF map of the composite specimen after heat treatment and (*f*) the corresponding grain size distribution in the heat-treated condition. Red and dashed-white arrows in (d), respectively, show the TiN particles at the grain centers and boundaries. Black arrows in (a), (b) and (e) show the build direction. (Figures have been adapted from Ref. [23]) (Color figure online).

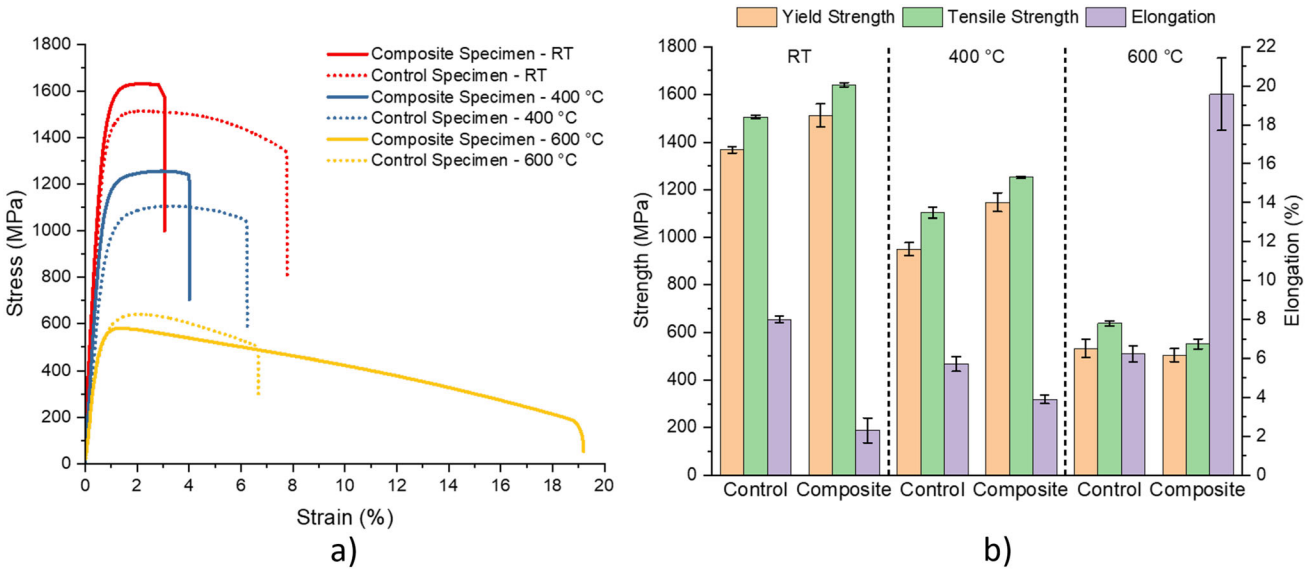

Fig. 3—(*a*) Stress *vs* strain diagrams of the control and composite specimens in H900 heat-treated condition at RT, 400 °C, 600 °C. (*b*) Overall yield strength, tensile strength, and elongation levels of all specimens at these temperatures.

inside the larger grains can be observed in Figure 5(c). The phase constitution was found to be dominantly ferrite with very small austenite grains detected at the grain boundaries of ferrite as shown in Figure 5(d).

Predicted phase amounts with respect to temperature under fast solidification conditions for the composite specimens are given in Figure 6(a). The equilibrium phase predictions are given in Figure 6(b) for the composite specimens. In the equilibrium case, ferrite is expected to

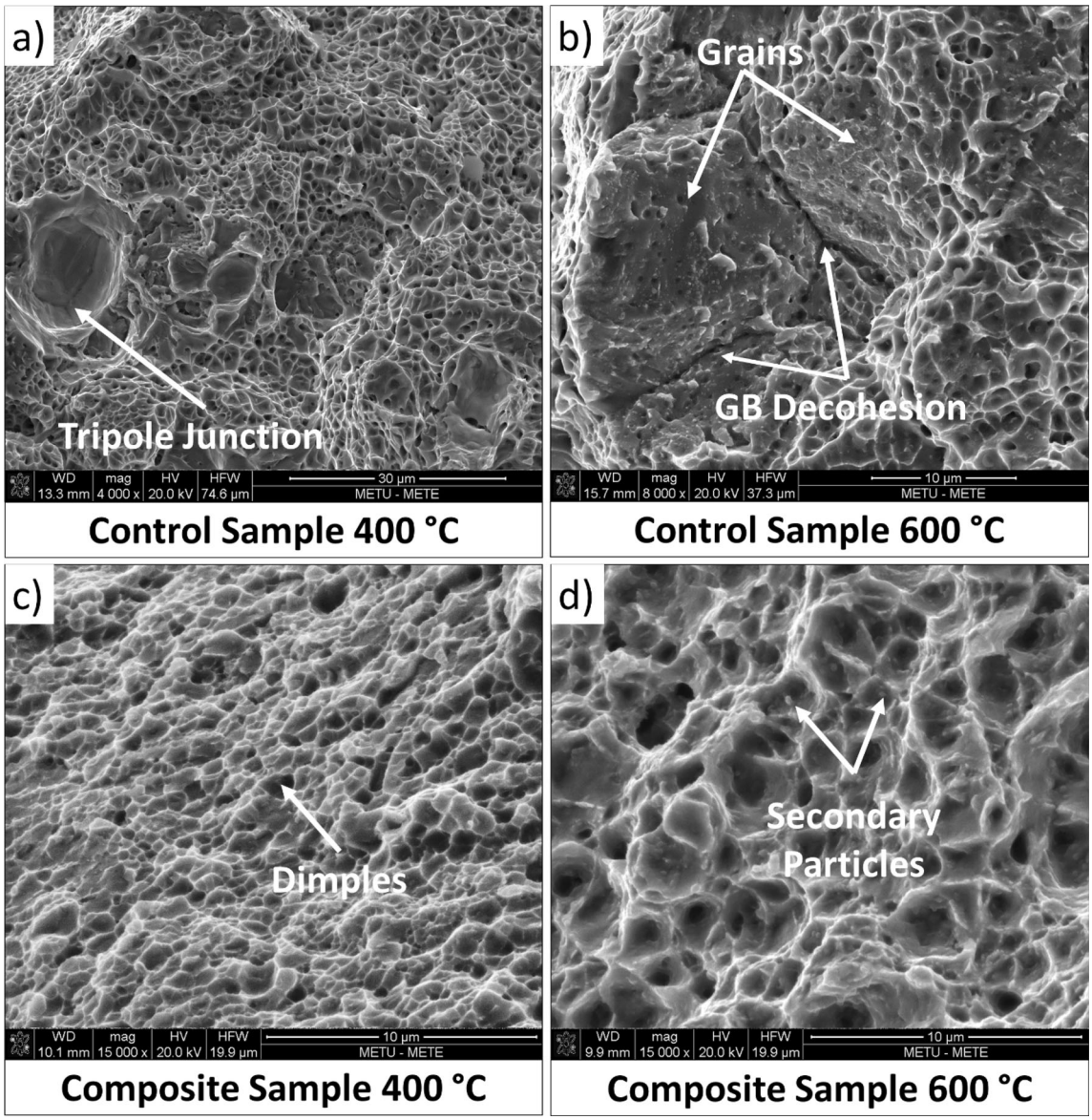

Fig. 4—Fracture surfaces of the control specimens tested at (*a*) 400 °C and (*b*) 600 °C, and the composite specimens tested at (*c*) 400 °C and (*d*) 600 °C.

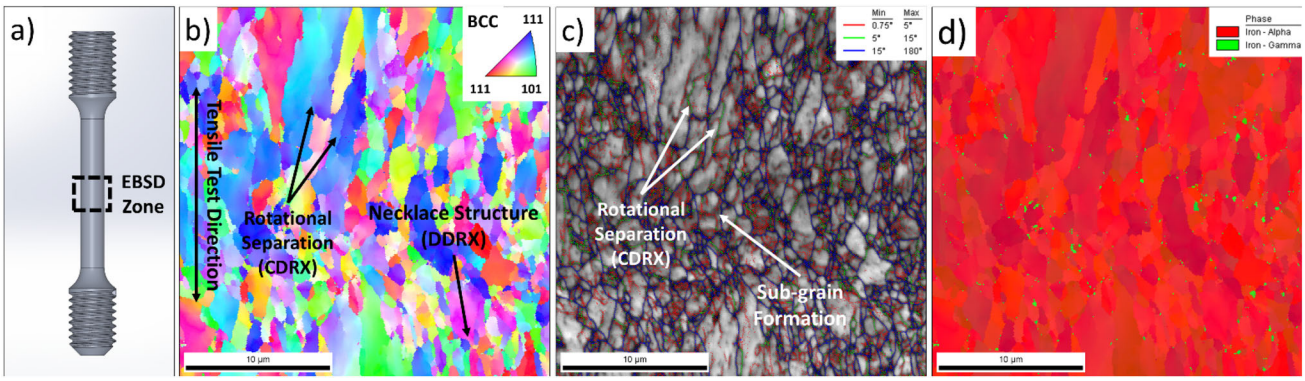

Fig. 5—(*a*) Schematic showing the zone where EBSD measurements were taken and corresponding (*b*) EBSD-IPF image, (*c*) grain boundary and (*d*) phase distribution maps for the composite tested at 600 °C.

form below 900 °C from austenite, and there is no austenite remaining below 450 °C. For both fast-cooling and equilibrium calculations, TiN is expected to form directly in the melt below 2100 °C and retain with the same volume percentage. There are other low-temperature phases shown in Figure 6(b), formation of which requires extended time to form in reality. Therefore, they are not considered in the following discussion as they were not detected by any means.

Figures 7(a) and (b) show the XRD spectra obtained at RT, 350 °C, and 600 °C. XRD spectrum at RT confirms the results of the EBSD analysis regarding the matrix, where BCC structure was identified at RT, with the only difference being the existence of some retained austenite in the XRD spectrum. Moreover, the expected presence of TiN is confirmed in all spectra. The rise in intensity of the FCC-(111) peak at 600 °C in Figure 7(b) indicates the formation of austenite at high temperatures as predicted in Figure 6(b). Due to the issues with atmospheric control during high temperature XRD measurements, some oxidation took place on the surface of the samples. Therefore, there are several unknown peaks appearing at 350 °C and 600 °C. As it is difficult to index these complex oxides in the presence of high temperature peak shifting, the main discussion will be held over the portion of the XRD spectra that is shown in Figure 7(b), where the evolution of the high-intensity ferrite, austenite and TiN peaks at different temperatures are depicted. Since the oxidation of the XRD samples does not change the main points claimed in the study, their discussion will not be held further.

IV. DISCUSSION

A. *Microstructure of the Composite Specimens*

As introduced in the results section, martensite forms upon solutionizing and aging heat treatment for the control specimens as observed in Figure 2(a). On the other hand, both EBSD and XRD results yield almost fully BCC structure at RT for the composite specimens. However, it is difficult to distinguish low-carbon martensite from ferrite *via* EBSD or XRD to very small deviations from the BCC lattice. The appearance of the composites is remarkably different than the control specimens after heat treatment, where the martensite blocks are not visible in the later, but grains of a typical nucleation-growth type formation are seen. Yet, similar studies that utilized TiN for martensitic steels, such as H13 tool steel observe the martensite blocks under EBSD.[33] On the other hand, when TiN is used for grain refining ferritic stainless steels, an appearance much closer to Figures 2(b) and (d) is obtained.[32] Therefore, it was concluded that the microstructure of the composite specimens consists of ferrite instead of martensite. It is hypothesized that this behavior was due to the accelerated kinetics of α-ferrite formation [the stable phase under equilibrium at RT according to Figure 6(b)] due to the TiN addition. TiN lowered the nucleation barrier for α-ferrite formation both by refining the prior austenite grain size and directly acting as a nucleant for α-ferrite. These changes rendered the cooling rates under pressurized argon insufficient to form martensite. The fact that the microstructures are nearly identical for as-built and heat-treated control specimens, the latter of which were completely austenitized and argon cooled, hints that the observed BCC phase in as-built composite specimens is the result of α-ferrite formation rather than δ-ferrite retention (austenite bypassing) as in other studies involving 17-4 PH stainless steel.[5,12] Overall, the martensitic microstructure of the control specimens hardened by the Cu-rich precipitates has been exchanged with the fine-grained α-ferritic microstructure of the composite specimens hardened by TiN particles, as well as Cu-rich precipitates in the heat-treated condition. Conformingly, TEM observations in the previous study of the authors on the same material system show that the high hardness of the as-built composite specimens can be

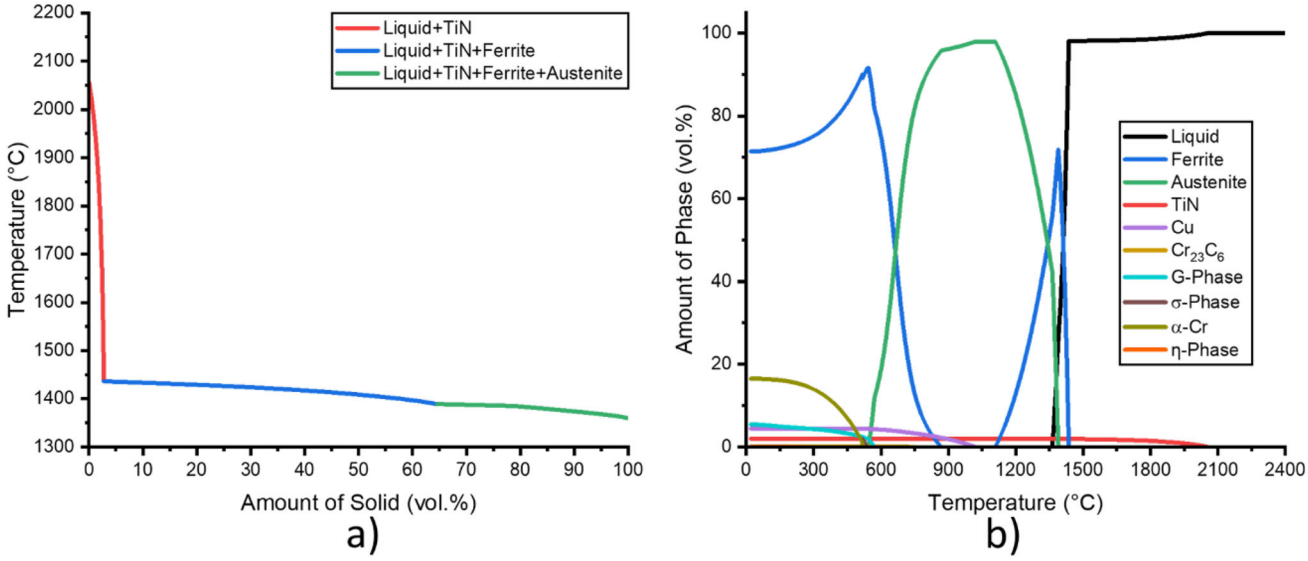

Fig. 6—Phase amounts expected with respect to temperature under (*a*) fast solidification conditions and (*b*) under equilibrium.

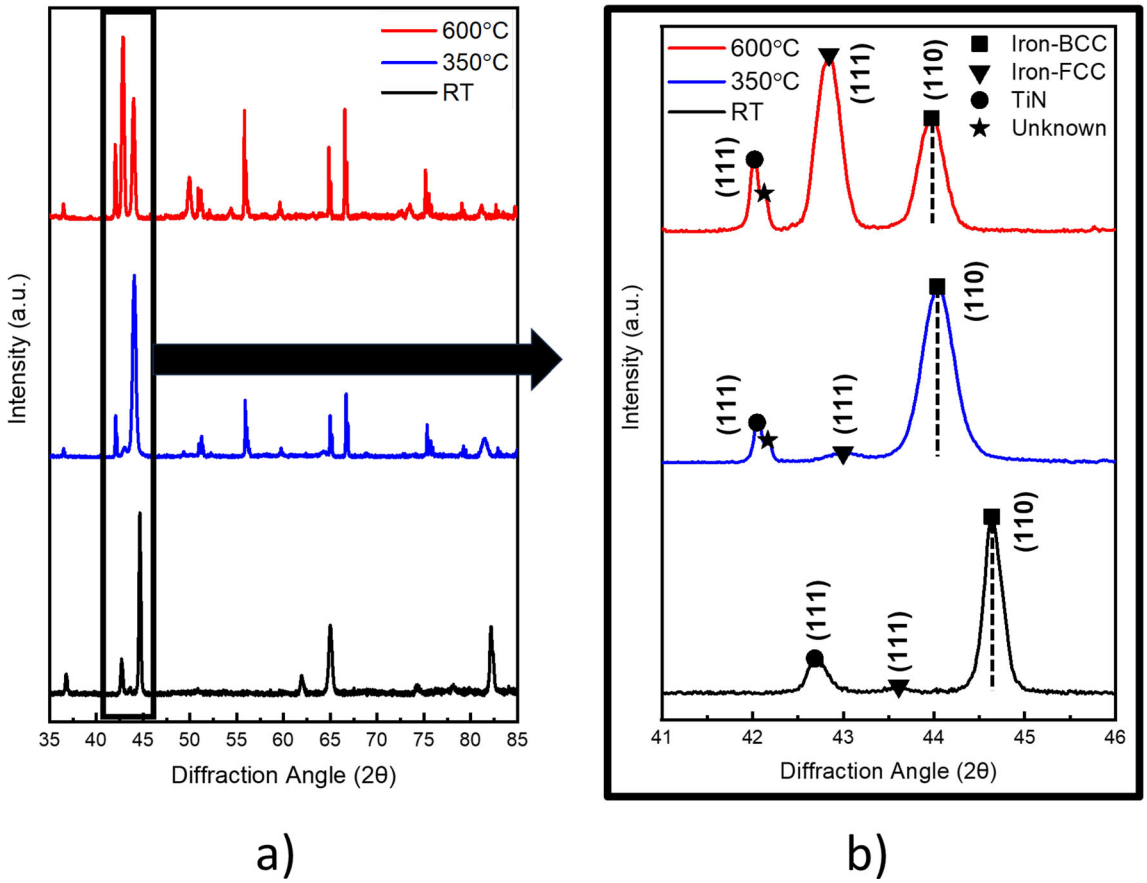

Fig. 7—(*a*) Full and (*b*) zoom-in view of the X-ray diffraction spectra collected from the composite specimens at RT, 350 °C, and 600 °C.

attributed to the fine grain size, dispersion strengthening due to nano-TiN particles and the high density of dislocations associated with the particles.[23]

B. *Tensile Behavior at Room Temperature and 400 °C*

A horizontal stress-strain curve is observed with limited strain hardening [see Figure 3(a)] for the RT tensile tests, where the curve reaches a stable and balanced stress level after yielding. As shown in Figure 3(b), a similar behavior was observed for the samples tested at 400 °C with lower strength levels. This can be attributed to the dynamic recovery processes taking place during the tensile deformation at elevated temperatures, which cause annihilation of dislocations created during deformation.[34] The interplay between strain hardening due to the deformation is compensated by the recovery, thus, a steady stress-strain diagram at lower stress levels is maintained until fracture.

As shown in the stress-strain diagrams of the control specimens in Figure 3(a), it has been observed that the ductility drops at high temperatures instead of increasing, and this has been related to intergranular dimpled mode of fracture following the observations in Figures 4(a) and (b), for both 400 °C and 600 °C, respectively. GB decohesion in one of the fracture surfaces of the control samples is shown in Figure 4(b), where the grains are directly visible with fracture dimples on them, together with the tripole junctions left behind. As it was shown in Figure 2(a), the microstructure of the control specimens was martensitic after heat treatment, where there were no directly observable grains, but rather martensite blocks and sub-blocks. Therefore, it can be evaluated that the observed grains in Figure 4(b) may belong to prior-austenite grain boundaries.

Although having a ductile appearance due to the dimples, dimpled intergranular fracture yields low macroscopic ductility. This mode of fracture is often associated with GB segregation of interstitial elements, presence of secondary particles at the GBs and particle-matrix decohesion at GBs for precipitation hardened alloys *etc.*[35] Grain boundary cohesion strength is known to decrease with increasing temperature, where grain boundary cavitation driven fracture occurs by various mechanisms proposed above, and larger grain sizes amplify the loss in grain boundary strength.[36] Similarly, Li *et al.* reported dimpled intergranular fracture for martensitic heat-resistant steels at elevated temperatures, where earlier onset of dynamic recrystallization and finer grain size were effective at controlling the propagation of intergranular cracks.[37] There have been various mechanisms proposed for intergranular dimpled fracture, and often there are more than one active mechanism as stated above. Therefore, the exact nature of the dimpled intergranular fracture of the

control specimen requires further investigation in the future, yet explains the observed low-ductility behavior.

On the other hand, the composite specimens show the features of a typical ductile fracture for both temperatures as presented in Figures 4(c) and (d), where the dimples on the fracture surface and the secondary particles at the dimple centers are seen. Considering the remarkable difference between the two samples without any change in the alloy composition (TiN particles do not alter the composition of the matrix), the change in fracture behavior can be attributed to the grain boundary strengthening due to the smaller grain size of the composite specimens.

C. *Tensile Behavior at 600 °C and the Role of Microstructure*

As shown in Figure 3(b), there has been approximately two-fold reduction in the strength levels at 600 °C compared to 400 °C. This result was expected as Cu-rich precipitates undergo significant coarsening at this temperature.[2] Both specimens exhibit strain softening upon yielding at 600 °C, where stress-strain diagrams have a negative slope after ultimate tensile strength (UTS) as seen in Figure 3(a). However, the control specimens did not show extensive elongation due to the intergranular dimpled fracture discussed previously. On the other hand, the composite specimens, despite having slightly lower strength compared to the control specimens, have shown five times higher ductility at 600 °C compared to 400 °C [see Figure 3(b)]. Considering the strain softening behavior after the peak stress seen in Figure 3(a), and the fact that 600 °C corresponds to a homologous temperature of about 0.5 (half of the melting point in K) for the alloy under consideration, dynamic recrystallization (DRX) appears to be responsible of the lower strength and higher elongation values. Since the softening by the stress-free grains created during dynamic recrystallization overcomes the strain hardening effect of dislocation formation during deformation, the strain softening behavior has been observed overall. It is known that smaller grain sizes promote an earlier stress onset of dynamic recrystallization due to the increased grain boundary area, *i.e.,* recrystallized grain nucleation zones.[38,39] Moreover, it should be noted that the initial dislocation density of the composite should have been higher than the control specimen, since TiN particles would generate more dislocations upon cooling after heat treatment.[40] Therefore, the composite, which has smaller grains and presumably higher initial dislocation density, exhibited a lower peak strength at higher temperature compared to the control specimen with a significant jump in elongation because of DRX that continuously provides deformable, stress-free grains.

Although the above-mentioned DRX hypothesis fits the observations in stress-strain diagrams in Figure 3(a) and the initial microstructure of the composite specimens, one point must be clarified. It is known that high stacking fault energy (SFE) materials, such as α-ferrite usually soften by dynamic recovery (DRV), where nucleation-driven dynamic recrystallization (DRX), also called discontinuous DRX (DDRX), does not often occur due to the increased need for driving force (deformation). However, continuous DRX (CDRX) can take place for high-SFE materials at elevated temperatures.[38,41] Although the exact mechanism is not well-understood, CDRX occurs by the successive reorientation and separation of sub-grains into grain boundaries by deformation.[38,41] Such rotational separation of sub-grains for the composite specimen can be observed in Figures 5(b) and (c), where sub-grain boundary misorientation starts to increase above 5 deg [shown in green in Figure 5(c)], suggesting that some CDRX takes place. Nonetheless, the equiaxed grains having very distinct orientations indicate the occurrence of a nucleation-driven recrystallization as well. DDRX is usually characterized by a necklace structure, an example of which can be observed in Figure 5(b), where smaller grains nucleate around the pre-existing grains.[38] The occurrence of DDRX in this case may be explained by the equilibrium phase composition at 600 °C. As can be seen from the figure, approximately 15 wt pct austenite must be present at 600 °C. Considering that TiN particles, as inoculants, would also accelerate the kinetics of austenite formation, austenite must have been present in the alloy during tensile tests at 600 °C. Therefore, the low-SFE austenite grains could have accommodated DDRX at this temperature. Nevertheless, the newly formed grains appear rather small, as TiN particles have also inhibited their growth after formation. TiN addition thus seems to have accelerated the initial recrystallization (nucleation) kinetics, while inhibiting growth.

In order to support this claim, high temperature XRD measurements have been conducted, results of which are shown in Figures 7(a) and (b). As observed in Figure 7(b), (110)-BCC peak shifts toward lower angles from RT to 350 °C due to lattice expansion with temperature. At RT and 350 °C, there is a negligible amount of austenite. However, at 600 °C, the intensity of the (111)-FCC austenite peak rises even above the (110)-BCC peak due to austenite formation. Moreover, from 350 °C to 600 °C, there is almost no shift in the (110)-BCC peak. This is because of the formation of austenite, which has a smaller volume than martensite, thus, compensating for the lattice expansion due to the temperature increase. Therefore, as predicted by the CALPHAD predictions in Figure 7(b), austenite exists during the tensile tests at 600 °C. Upon cooling, austenite back-transformed into ferrite explaining why the structure consists of mostly ferrite (Iron-BCC) with some retained austenite (Iron-FCC) after the tests, as shown in Figure 5(d). Observation of very small-sized austenite grains in Figure 5(d) also supports the above-mentioned claim.

Consequently, it can be said that both DRV and CDRX of the ferrite and DDRX of austenite took place during the hot tension test of the composite at 600 °C, which explains the extensive ductility observed at this temperature for the composite specimens. It also resulted in slightly lower onset of yielding for the composite specimens due to the smaller grain size and TiN particles aiding the formation of austenite.

However, the intergranular dimpled fracture seen in the control specimens has been avoided thanks to the freshly formed austenite grains that resulted in three times higher ductility compared to the composite specimens.

V. CONCLUSION

Nano-TiN incorporation to LPBF processed 17-4 PH stainless steel remarkably improved the high temperature strength at 400 °C, which is usually the limiting temperature for use of 17-4 PH stainless steel due to rapidly decaying strength above this limit caused by precipitate coarsening. At 600 °C, as the homologous temperature of 0.5 T_m is reached, matrix-dominated softening phenomena, such as dynamic recovery and dynamic recrystallization eliminate the additional strength gained by TiN incorporation, yet, with a threefold increase in ductility. The increase in ductility allowed the material to avoid intergranular dimpled fracture observed in the unreinforced control specimens. It has been concluded that the metallurgical and physical characteristics of the matrix play a crucial role on the limit at which dispersion strengthening can be operative. Although the matrix material sets an upper bound in the end, it has been shown that fine and uniformly distributed dispersoid particles in the matrix can be both used to increase strength at the regular operating temperatures and to ensure sufficient ductility at higher temperatures.

ACKNOWLEDGMENTS

The authors thank Central Laboratory of Middle East Technical University in Ankara, Turkey for their support in materials characterization by SEM. The authors also thank Central Laboratory of Eskisehir Osmangazi University in Eskisehir, Turkey for their support in XRD characterization.

FUNDING

Open access funding provided by the Scientific and Technological Research Council of Türkiye (TÜBİTAK). This research did not receive any specific grant from funding agencies in the public, commercial, or not-for-profit sectors.

DATA AVAILABILITY

Data not available due to commercial restrictions.

COMPETING INTERESTS

The authors declare that they have no known competing financial interests or personal relationships that could have appeared to influence the work reported in this paper.

OPEN ACCESS

This article is licensed under a Creative Commons Attribution 4.0 International License, which permits use, sharing, adaptation, distribution and reproduction in any medium or format, as long as you give appropriate credit to the original author(s) and the source, provide a link to the Creative Commons licence, and indicate if changes were made. The images or other third party material in this article are included in the article's Creative Commons licence, unless indicated otherwise in a credit line to the material. If material is not included in the article's Creative Commons licence and your intended use is not permitted by statutory regulation or exceeds the permitted use, you will need to obtain permission directly from the copyright holder. To view a copy of this licence, visit http://creativecommons.org/licenses/by/4.0/.

REFERENCES

1. J.K.L. Lai, K.H. Lo, and C.H. Shek: *Stainless Steels: An Introduction and Their Recent Developments*, Bentham eBooks, Dubai, 2012.
2. J.H. Wu and C.K. Lin: *J. Mater. Sci.*, 2003, vol. 38, pp. 965–71.
3. C.N. Hsiao, C.S. Chiou, and J.R. Yang: *Mater. Chem. Phys.*, 2002, vol. 74, pp. 134–42.
4. R. Bhambroo, S. Roychowdhury, V. Kain, and V.S. Raja: *Mater. Sci. Eng. A*, 2013, vol. 568, pp. 127–33.
5. M. Alnajjar, F. Christien, K. Wolski, and C. Bosch: *Addit. Manuf.*, 2019, vol. 25, pp. 187–95.
6. A. Ozsoy, E. Yasa, M. Keles, and E.B. Tureyen: *J. Manuf. Process.*, 2021, vol. 68, pp. 910–22.
7. D.J. Shaffer, A.E. Wilson-Heid, J.S. Keist, A.M. Beese, and T.A. Palmer: *Mater. Sci. Eng. A*, 2021, vol. 817, p. 141363.
8. M.S. Moyle, N. Haghdadi, X.Z. Liao, S.P. Ringer, and S. Primig: *J. Mater. Sci. Technol.*, 2022, vol. 117, pp. 183–95.
9. E.A. Lass, M.R. Stoudt, and M.E. Williams: *Metall. Mater. Trans. A*, 2019, vol. 50A, pp. 1619–24.
10. H. Eskandari, H.R. Lashgari, L. Ye, M. Eizadjou, and H. Wang: *Mater. Today Commun.*, 2022, vol. 30, p. 103075.
11. Z. Yu, Z. Chai, C. Yu, J. Chen, J. Xu, and H. Lu: *Mater. Sci. Eng. A*, 2022, vol. 849, p. 143527.
12. S. Vunnam, A. Saboo, C. Sudbrack, and T.L. Starr: *Addit. Manuf.*, 2019. https://doi.org/10.1016/j.addma.2019.100876.
13. S. An, D.-R. Eo, H. Lim, I. Sohn, and K. Choi: *Addit. Manuf.*, 2024, vol. 91, p. 104339.
14. I. Vysotskiy, S. Malopheyev, I. Zuiko, S. Mironov, and R. Kaibyshev: *Mater Charact*, 2022, vol. 194, p. 112405.
15. W.H. Yu, S.L. Sing, C.K. Chua, C.N. Kuo, and X.L. Tian: *Prog. Mater. Sci.*, 2019, vol. 104, pp. 330–79.
16. B. AlMangour, D. Grzesiak, and J.M. Yang: *Powder Technol.*, 2018, vol. 326, pp. 467–78.
17. B. Li, B. Qian, Y. Xu, Z. Liu, J. Zhang, and F. Xuan: *Mater. Sci. Eng. A*, 2019, vol. 745, pp. 495–508.
18. S. Dadbakhsh, R. Mertens, K. Vanmeensel, G. Ji, and J.P. Kruth: *Sci. Rep.*, 2020. https://doi.org/10.1038/s41598-020-67434-3.
19. M. Lorusso, A. Aversa, D. Manfredi, F. Calignano, E.P. Ambrosio, D. Ugues, and M. Pavese: *J. Mater. Eng. Perform.*, 2016, vol. 25, pp. 3152–60.
20. B. Li, L. Zhang, Y. Xu, Z. Liu, B. Qian, and F. Xuan: *Powder Technol.*, 2019, vol. 360, pp. 509–21.
21. X. Li, D. Yi, B. Liu, J. Zhang, X. Yang, C. Wang, Y. Feng, P. Bai, Y. Liu, and M. Qian: *Mater. Sci. Eng. A*, 2020, vol. 798, p. 140099.
22. K.U. Kainer: *Metal Matrix Composites: Custom-Made Materials for Automotive and Aerospace Engineering*, Wiley-VCH Verlag GmbH & Co. KGaA, Weinheim, 2006.
23. A. Ozsoy, E. Aydogan, and A.F. Dericioglu: *Mater. Sci. Eng. A*, 2021, vol. 836, p. 142574.
24. ASTM-E8m: https://doi.org/10.1520/E0008_E0008M-21.

25. ASTM-A564: ASTM Int., 2010, pp. 1–7.
26. N. Saunders, U.K.Z. Guo, X. Li, A.P. Miodownik, and J.-P. Schillé: *JOM*, 2003, vol. 55, pp. 60–65.
27. H.L. Lukas, J. Weiss, and E.-T. Henig: *Calphad*, 1982, vol. 6, pp. 229–29.
28. T. Inada: Massachusetts Institute of Technology, 1999.
29. D.A. Arvola: Missouri University of Science and Technology, 2018, p. 170.
30. D.A. Arvola, S.N. Lekakh, R.J. O'Malley, and L.N. Bartlett: *Int. J. Met.*, 2019, vol. 13, pp. 504–18.
31. Y. Wang, Z. Liu, Y. Zhou, X. Yang, J. Tang, X. Liu, J. Li, and G. Le: *Mater. Sci. Eng. A*, 2021, vol. 814, p. 141220.
32. A. Durga, N.H. Pettersson, S.B.A. Malladi, Z. Chen, S. Guo, L. Nyborg, and G. Lindwall: *Scripta Mater.*, 2021, vol. 194, p. 113690.
33. Q. Tan, H. Chang, Y. Yin, F. Wang, D. Huang, G. Liang, T. Wu, M. Yan, X. Cheng, and M.-X. Zhang: *Scripta Mater.*, 2022, vol. 219, p. 114874.
34. F. Abe, ed.: *Creep-Resistant Steels*, 1st ed. CRC Press, Boca Raton, FL, 2008.
35. K.L. Edwards: *Mater. Des.*, 2004, vol. 25, pp. 735–36.
36. C.L. Briant and S.K. Banerji: *Int. Met. Rev.*, 1978, vol. 23, pp. 164–99.
37. J. Li, B. Jiang, C. Zhang, L. Zhou, and Y. Liu: *Mater. Sci. Eng. A*, 2016, vol. 677, pp. 274–80.
38. K. Huang and R.E. Logé: *Mater. Des.*, 2016, vol. 111, pp. 548–74.
39. M. El Wahabi, L. Gavard, F. Montheillet, J.M. Cabrera, and J.M. Prado: *Acta Mater.*, 2005, vol. 53, pp. 4605–12.
40. M.F. Ashby: *Philos. Mag.*, 1966, vol. 14, pp. 1157–78.
41. H.A. Derazkola, E.G. Gil, A. Murillo-Marrodán, and D. Méresse: *Metals*, 2021. https://doi.org/10.3390/met11040572.

Publisher's Note Springer Nature remains neutral with regard to jurisdictional claims in published maps and institutional affiliations.